

***Original***

Becherer, J.; Floeser, G.; Umlauf, L.; Burchard, H.:  
**Estuarine Circulation vs Tidal Pumping: Sediment Transport  
in a Well-Mixed Tidal Inlet**  
Journal of Geophysical Research : Oceans (2016) AGU

DOI: 10.1002/2016JC011640

## RESEARCH ARTICLE

10.1002/2016JC011640

## Key Points:

- Not estuarine circulation, but tidal pumping dominates SPM transport in well-mixed estuarine systems
- First direct observations of estuarine circulation in the Wadden Sea
- Wind forcing has a substantial influence on estuarine circulation and SPM transport

## Correspondence to:

J. Becherer,  
jbecherer@coas.oregonstate.edu

## Citation:

Becherer, J., G. Flöser, L. Umlauf, and H. Burchard (2016), Estuarine circulation versus tidal pumping: Sediment transport in a well-mixed tidal inlet, *J. Geophys. Res. Oceans*, 121, 6251–6270, doi:10.1002/2016JC011640.

Received 11 JAN 2016

Accepted 10 JUN 2016

Accepted article online 16 JUN 2016

Published online 23 AUG 2016

## Estuarine circulation versus tidal pumping: Sediment transport in a well-mixed tidal inlet

Johannes Becherer<sup>1,2</sup>, Götz Flöser<sup>3</sup>, Lars Umlauf<sup>2</sup>, and Hans Burchard<sup>2</sup>

<sup>1</sup>College of Earth, Ocean, and Atmospheric Sciences, Oregon State University, Corvallis, Oregon, USA, <sup>2</sup>Leibniz Institut für Baltic Sea Research Warnemünde, Rostock, Germany, <sup>3</sup>Helmholtz Zentrum Geesthacht, Geesthacht, Germany

**Abstract** High-resolution water column observations have been carried out in the Wadden Sea to understand suspended particulate matter (SPM) transport in well-mixed tidal channels. These observations include more than 4000 consecutive CTD, microstructure shear and turbidity profiles from a free-falling microstructure probe, as well as velocity data from an ADCP and SPM samples for calibration. A horizontal density gradient was established by a landward temperature gradient built up during an extraordinarily warm and calm spring season. Tidal averaging along  $\sigma$ -layers (relative depth) provides the first direct observations of along-channel estuarine circulation in the Wadden Sea, with net inflow near the bottom and outflow near the surface. Increased westerly (up-estuary) winds during the second part of the campaign weakened and eventually even reversed estuarine circulation and yielded a net barotropic eastward transport. SPM concentrations showed a strong quarter-diurnal signal with maxima near full flood and full ebb and were generally lower during the calm period and increased during the windy period, mainly due to wave-related resuspension over nearby intertidal flats. The sediment flux analysis was based on a decomposition of the vertically integrated SPM flux into a barotropic advective component, an estuarine circulation component and a tidal pumping component. As a result, tidal pumping (due to ebb-dominance weakly seaward) dominated the SPM flux during calm conditions, whereas barotropic advection dominated the strong landward SPM flux during the windy period. Along-channel estuarine circulation is found to be of minor importance for the net SPM transport in such well-mixed systems.

## 1. Introduction

Estuarine circulation is a well-known feature of horizontally stratified systems in the coastal ocean. At the bottom, the residual currents are directed landward and seaward at the surface. Originally, this characteristic exchange flow was thought to be exclusively associated with the gravitational circulation caused by the horizontal density gradient [Hansen and Rattray, 1965].

In tidally energetic systems however, a number of additional processes can be of great importance for the generation of estuarine exchange flows. These processes can be associated with internal tidal asymmetry [Jay and Musiak, 1994; Stacey, 1996] or lateral rectification of along-channel momentum [Lerczak and Geyer, 2004; Becherer et al., 2015; Schulz et al., 2015]. Both mechanisms act in a similar way by generating an ebb-flood asymmetry in the vertical profile of the along-channel velocity, which yields a residual flow typically oriented in the same direction as classical gravitational circulation [Lerczak and Geyer, 2004]. Especially in well-mixed highly energetic systems these processes are often more important for the generation of estuarine circulation than gravitational circulation [Burchard and Hetland, 2010; Burchard et al., 2011; Becherer, 2014; Schulz et al., 2015].

The Wadden Sea of the German Bight in the south-eastern North Sea (see Figure 2) provides a natural laboratory for studying tidally energetic flow interacting with lateral buoyancy gradients. Based on a three-dimensional model of a Wadden Sea basin, Burchard et al. [2008] showed the necessity of a horizontal density gradient to generate an effective suspended particulate matter (SPM) import into the system. These authors also concluded that estuarine circulation may be an important driver for sediment transport into the Wadden Sea.

Flöser et al. [2011] show a characteristic asymmetry between average ebb and flood profiles of the along-channel current velocity, providing a first observational hint for the presence of tidal straining. Becherer

*et al.* [2011] finally provided direct observational evidence for the relevance of tidal straining in the Wadden Sea by means of a characteristic ebb-flood asymmetry in vertical stratification and turbulence distribution. However, at a different location in the channel, these authors also found a strong unexpected vertical stratification during full flood tide, which could not be explained by longitudinal buoyancy gradients. Based on observations [Becherer *et al.*, 2015] and a modeling study [Purkiani *et al.*, 2015], it could be shown that this flood tide stratification is a characteristic feature of tidal flows in the Wadden Sea that is associated with lateral dynamics. Becherer *et al.* [2015] furthermore highlighted the potential importance of asymmetric lateral circulation for the generation of estuarine circulation. They found these processes to be more important than tidal straining or gravitational circulation. Despite the detailed investigation of different potential drivers of estuarine circulation, only little observational evidence exists for longitudinal exchange flow in the Wadden Sea [Becherer *et al.*, 2011; Flöser *et al.*, 2013; Becherer, 2014]. Closing this gap is one of the aims of the present study.

Although earlier studies suggested that estuarine circulation is potentially an important driver of sediment transport in the Wadden Sea [Burchard *et al.*, 2008], there were no attempts to quantify its effect based on measurement data so far. A recent study [Burchard *et al.*, 2013] based on an idealized model investigated the relative contribution of estuarine circulation to the overall sediment transport for parameter combinations that include typical Wadden Sea conditions. The authors used a decomposition of the total sediment flux into an advective flux and a tidal pumping flux due to covariance between SPM concentration and current velocity. A similar decomposition was introduced before by Scully and Friedrichs [2007] and Geyer *et al.* [2001]. All these authors found that in many situations the tidal pumping flux might be more important than the advective flux, although the latter contains the estuarine exchange flow as a driver. A similar conclusion was recently drawn by Schulz and Umlauf [2016], who investigated the residual transport of suspended material due to tidal straining near sloping topography.

The major aim of our study is to investigate the relative contribution of estuarine circulation to sediment transport in well-mixed estuarine systems, taking a recent data set from the German Wadden Sea as an example. To this end, we use a similar decomposition as Geyer *et al.* [2001], Scully and Friedrichs [2007], and Burchard *et al.* [2013]. Here however, we go one step further and split the advective flux into a barotropic flux and a pure estuarine exchange flow component. A description of the flux decomposition can be found in section 2.

As the basis of our analysis we present in section 3.3, a unique data set of more than 4800 vertical microstructure profiles of turbulence, density, and sediment that cover several consecutive tidal cycles with a temporal resolution of less than 2 min on average. This data set was obtained during a longer survey that is briefly described in section 3.1.

By applying a tidally averaging procedure to ship based ADCP data, we are able to quantify estuarine circulation in the Wadden Sea by means of direct observations (section 4). Combining all the available data, we investigate the relative contributions of the different drivers (estuarine circulation, tidal pumping, wind, and lateral circulation) to sediment transport in section 5. The general implications of our findings, the limitations of our observation-based investigations, and a brief discussion on the potential role of lateral circulation in sediment transport are presented in section 6.

## 2. Methods

### 2.1. $\sigma$ -Layers

In this paper, we are primarily interested in tidally averaged volume and SPM fluxes. For systems where the tidal amplitude is not negligible compared to the water depth,  $H$ , it is necessary to account for the change in sea-surface elevation,  $\eta(t)$ , to obtain representative values for the tidal average. In this regard, we introduce  $M$  equidistant vertical layers,  $\sigma$ -layers, which change their thickness following the sea surface,

$$h_{\sigma}(t) = \frac{1}{M}(H + \eta(t)). \quad (1)$$

Here we use 20 vertical layers ( $M = 20$ ). The  $z$ -coordinate of the center of each  $\sigma$ -layer is given by

$$z_{\sigma}(t) = \frac{\sigma - 0.5}{M} (H + \eta(t)) - H \quad \sigma = 1 \dots M. \tag{2}$$

By interpolation along the  $\sigma$ -layer grid, we are able to fill smaller temporal gaps in the data, to obtain a continuous time series necessary to perform time averages,

$$X(t, z) \rightarrow X_{\sigma}(t). \tag{3}$$

**2.2. Averaging Procedure**

Any scalar quantity,  $X$ , can be decomposed into its average,  $\langle X \rangle_A$ , and a remaining part,  $\{X\}_A$ ,

$$X = \langle X \rangle_A + \{X\}_A, \tag{4}$$

where A indicates the specific averaging procedure. In this paper, we use two different kind of averages, a tidal average  $\langle X \rangle_{\tau}$  and a vertical average  $\langle X \rangle_{\sigma}$ .

The tidal average is calculated along  $\sigma$ -layers, according to

$$\langle X_{\sigma} \rangle_{\tau} = \left[ \int_{\tau - T_{M2}}^{\tau + T_{M2}} h_{\sigma}(t) dt \right]^{-1} \int_{\tau - T_{M2}}^{\tau + T_{M2}} X_{\sigma}(t) h_{\sigma}(t) dt, \tag{5}$$

where  $T_{M2} = 44714$  s denotes the  $M_2$ -tidal period and  $\tau$  the center of the averaging window. We choose two tidal periods for the window width here, in order to account for the daily periodicity of the tidal currents. Note that  $\langle X_{\sigma} \rangle_{\tau}$  does not directly depend on  $t$ , but on the averaging window characterized by  $\tau$ . This formal distinction is necessary in order to ensure that

$$\langle \langle X_{\sigma} \rangle_{\tau} \rangle_{\tau} = \langle X_{\sigma} \rangle_{\tau}. \tag{6}$$

Consequently, we define the deviation from the mean as

$$\{X_{\sigma}\}_{\tau}(t) = X_{\sigma}(t) - \langle X_{\sigma} \rangle_{\tau}, \tag{7}$$

which yields another important property of this particular averaging procedure,

$$\langle \{X_{\sigma}\}_{\tau} \rangle_{\tau} = 0. \tag{8}$$

Note that for any given  $\tau$ ,  $\{X_{\sigma}\}_{\tau}(t)$  will be different, such that  $\langle \{X_{\sigma}\}_{\tau} \rangle_{\tau'} = 0$  is only true for  $\tau = \tau'$ .

In the framework of the  $\sigma$ -layer grid, the vertical average reads as

$$\langle X \rangle_{\sigma} = \frac{1}{M} \sum_{\sigma=1}^M X_{\sigma}, \tag{9}$$

which has properties similar to (6) and (8),

$$\langle \langle X \rangle_{\sigma} \rangle_{\sigma} = \langle X \rangle_{\sigma}; \quad \langle \{X\}_{\sigma} \rangle_{\sigma} = 0. \tag{10}$$

Although all the quantities discussed in the following are interpolated along  $\sigma$ -layers, we omit the subscript  $\sigma$  for convenience.

**2.3. Sediment Flux Decomposition**

By making use of (5), (6), and (8), it is possible to decompose the tidally averaged sediment flux along a  $\sigma$ -layer,

$$\langle cu \rangle_{\tau} = \langle (\langle u \rangle_{\tau} + \{u\}_{\tau}) (\langle c \rangle_{\tau} + \{c\}_{\tau}) \rangle_{\tau} \tag{11}$$

$$= \langle c \rangle_{\tau} \langle u \rangle_{\tau} + \langle \{c\}_{\tau} \{u\}_{\tau} \rangle_{\tau}, \tag{12}$$

where  $c$  denotes the sediment concentration and  $u$  the along-channel velocity. In this decomposition,  $\langle c \rangle_{\tau} \langle u \rangle_{\tau}$  is referred to as advective flux and  $\langle \{c\}_{\tau} \{u\}_{\tau} \rangle_{\tau}$  as tidal pumping. Similar decompositions have been used in previous studies [Geyer et al., 2001; Scully and Friedrichs, 2007; Burchard et al., 2013; McSweeney et al., 2016].

To obtain the sediment flux across the entire water column, we use (9) to average (11) in the vertical and multiply by the tidally averaged total water depth  $\langle D \rangle_\tau = M \int_{\tau-T_{M2}}^{\tau+T_{M2}} h_\sigma dt$ . This procedure yields the following decomposition of the total sediment flux,

$$\mathcal{F}_{tot} = \langle D \rangle_\tau \langle \langle cu \rangle_\tau \rangle_\sigma, \tag{13}$$

$$= \langle D \rangle_\tau \langle \langle c \rangle_\tau \langle u \rangle_\tau \rangle_\sigma + \langle D \rangle_\tau \langle \langle \{c\}_\tau \{u\}_\tau \rangle_\tau \rangle_\sigma, \tag{14}$$

$$= \underbrace{\langle D \rangle_\tau \langle c \rangle_{\tau,\sigma} \langle u \rangle_{\tau,\sigma}}_{\mathcal{F}_{bf}} + \underbrace{\langle D \rangle_\tau \langle \{c\}_\tau \{u\}_\tau \rangle_\sigma}_{\mathcal{F}_{exf}} + \underbrace{\langle D \rangle_\tau \langle \{c\}_\tau \{u\}_\tau \rangle_{\tau,\sigma}}_{\mathcal{F}_{tpf}}. \tag{15}$$

Here the advective flux is split further into a barotropic component referred to as the barotropic flux,  $F_{bf}$  and a component entirely due to the vertical exchange flow,  $F_{exf}$ . While the latter component is boiled down to the contribution of estuarine circulation,  $F_{bf}$  contains all contributions of residual barotropic flows, including river runoff, barotropic ebb-flood asymmetries, and wind stress. The remaining part in (15) is the tidal pumping flux,  $F_{tpf}$ , which is due to an intertidal correlation of the sediment concentration and the current velocity.

Note that former studies [Geyer *et al.*, 2001; Scully and Friedrichs, 2007; Sommerfield and Wong, 2011; McSweeney *et al.*, 2016] used a low-pass filter in order to distinguish between advection and tidal pumping. The advantage of the procedure presented here compared to the low-pass filter method is that we obtain a perfectly closed balance, which allows for the extended decomposition in (15). Only this way we are able to independently quantify the contribution of the exchange flow, the barotropic flow and the intertidal correlation component (tidal pumping). A more detailed comparison of both methods will be given in section 5.4.

#### 2.4. Instrumentation

Most of the quantities presented here have been measured with a free-falling microstructure profiler (MSS-90L from In-Situ Wassermesstechnik, ISW, Germany). While falling with an average speed of about  $0.35 \text{ m s}^{-1}$  the profiler is sampling at a frequency of 1024 Hz. The profiler is equipped with precision CTD-sensors from Sea and Sun Technology (SST, Germany), two airfoil shear probes (PNS06 from ISW, Germany), a turbidity sensor from Seapoint (USA), and a fast-response temperature sensor (FP07). For details on the profiler instrumentation, see *van der Lee and Umlauf* [2011]. The profiler CTD-data are averaged to 10 cm and the dissipation data to 50 cm vertical bins.

In addition to the profiler, we used a pumped CTD, which provides a reference for the profiler data. The pumped CTD is a multiprobe instrument equipped with sensors for temperature (Pt-100, Sea & Sun, Germany), conductivity (7 pole AMT sensor, Germany), pressure, turbidity, and a number of other sensors that have not been used in the current manuscript (fluorescence, transmission, pH, oxygen saturation, and photosynthetically active radiation).

To determine the sediment concentration in the water column, we used two turbidity sensors mounted on different platforms together with in situ water samples. One sensor was attached to the MSS90 profiler, which provides a set of turbidity data with high temporal and vertical resolution over the entire measurement period. A second sensor was mounted at the pumped CTD. Both sensors are of the same type from Seapoint. Attached to the pumped CTD, close to the turbidity sensor, was a hose connecting the subsurface inlet to an onboard pumping system supporting a flow rate of  $30 \text{ mL s}^{-1}$  to fill water bottles for sampling. One liter water samples are filtered on board over 4.7 cm Whatman GF/C filters, rinsed 3 times with deionized water in order to remove salt from the filter, and frozen to  $-18^\circ\text{C}$ . In the lab, samples were thawed, dried (3 h at  $100^\circ\text{C}$ ) and weighed. These samples were used to determine the suspended particulate matter (SPM) concentration by measuring the dry sediment weight. Neither the grain size distribution nor organic matter content has been analyzed.

The velocity data were measured with a ship mounted ADCP (RDI 1200 Hz). The ADCP data were rotated by  $12^\circ$  to obtain the along-channel and across-channel velocity component, respectively, with the coordinate system pointing along the channel into the Wadden Sea (see Figure 2).

A detailed description of the instrumentation can be found in *Becherer et al.* [2015].

2.5. Sediment Calibration

In order to translate the high-resolution profiler turbidity data into sediment concentrations, we first correlated the in situ samples with the CTD-turbidity probe, and in a second step the two different turbidity probes with each other. The first step is however not entirely straightforward. Figure 1a shows that the correlation of the CTD-turbidity  $Tu_0$  and the in situ sediment concentration,  $c$ , exhibits a correlation coefficient of only about 66%. The reason for this originates in a strong variation of the ratio  $c/Tu_0$  (Figure 1e).  $c/Tu_0$  varies between 2 and 4, sometimes increasing up to  $10 \text{ mg L}^{-1} \text{ ftu}^{-1}$ . A part of this variation can be explained by a periodic change of the grain size distribution of suspended sediment during a tidal cycle, where we expect a bigger fraction of large grain sizes during peak currents, which would consequently yield a larger ratio  $c/Tu_0$ . In support of this hypothesis, we find large values of  $c/Tu_0$  to coincide with large values of the bottom shear stress,  $\tau_b$  (Figure 1e).

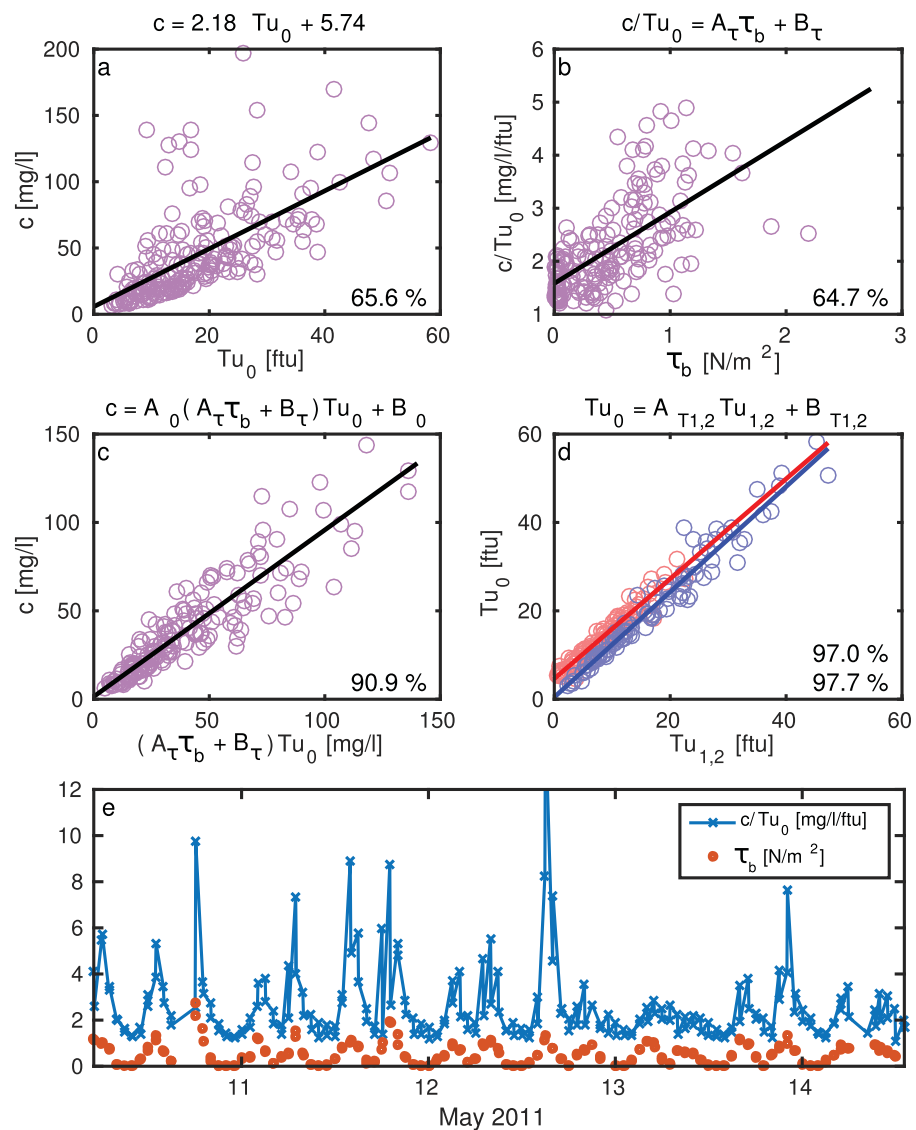


**Figure 1.** Sediment calibration. Shown are the correlations of (a) the CTD-mounted turbidity sensor ( $Tu_0$ ) and the in situ sediment concentration samples ( $c$ ), (b) the bottom shear stress ( $\tau_b$ ) and the ratio of  $Tu_0$  and  $c$ , (c) the  $\tau_b$ -corrected turbidity data and  $c$ , and (d) the CTD-mounted turbidity data and the corresponding profiler data. Note that we distinguish two periods, with different calibration coefficients for the profiler-mounted turbidity probe. The straight lines in Figures 1a–1d show the linear fit of the data, where the corresponding function are displayed above each figure. Numerical values of the fitting parameters can be found in Table 1. (e) A time series of the ratio of  $c/Tu_0$  and the bottom-shear stress,  $\tau_b$ , respectively.

**Table 1.** List of Correlation Parameters for (16)

| $A_0$ | $B_0$ (mg/L) | $A_\tau$ (mg m <sup>2</sup> /(L ftu N)) | $B_\tau$ (mg/(L ftu)) | $A_{T1}$ | $B_{T1}$ (ftu) | $A_{T2}$ | $B_{T2}$ (ftu) |
|-------|--------------|---|-----------------------|----------|----------------|----------|----------------|
| 0.94  | 1.50         | 1.34                                    | 1.58                  | 1.13     | 4.64           | 1.19     | 0.46           |

We calculate  $\tau_b$  based on the dissipation rates obtained with the shear probes of the vertical profiler, assuming a balance between dissipation and shear production of turbulent kinetic energy close to the bottom (for details see *Becherer et al.* [2015]). Alternatively, it would be possible to estimate  $\tau_b$  based on a logarithmic fit of the near bottom ADCP data, which we have not done here, since we found the microstructure estimates to be more consistent.

The diameter,  $D_s$ , of the eroded sediment is roughly proportional to  $\tau_b$ , the sediment concentration,  $c$ , scales approximately with  $D_s^3$ , and the turbidity with  $D_s^2$  [*Baker and Lavelle*, 1984]. Those relations indicate a linear correlation between  $\tau_b$  and  $c/Tu_0$ . In fact,  $\tau_b$  and  $c/Tu_0$  show a weak but significant linear correlation of about 65% (Figure 1b).

We use the correlation of  $\tau_b$  and  $c/Tu_0$  to incorporate the bottom shear stress in the correlation of  $Tu_0$  and the in situ sediment data,  $c$ . With about 91% the  $\tau_b$ -corrected CTD-turbidity is much better correlated to the sediment concentration than  $Tu_0$  alone (compare Figures 1a and 1c).

The correlation of  $Tu_0$  and the profiler-mounted turbidity probe is relatively straight forward. The only complication is that we need to distinguish two different periods ( $Tu_1$  and  $Tu_2$ ), since the sensitivity of the profiler-mounted sensor was changed on May 12 at 6 AM (see magenta line Figure 4). During both periods, the profiler sensor shows a large correlation of more than 97% to  $Tu_0$ , with slightly different coefficients for the two periods (Figure 1d).

By making use of the different correlations above, we obtain a sufficiently robust formula to translate profiler turbidity data into sediment concentrations,

$$c = A_0(A_\tau \tau_b + B_\tau)(A_{T1,2} Tu_{1,2} + B_{T1,2}) + B_0, \tag{16}$$

where the different constants are listed in Table 1.

### 3. Observations

#### 3.1. Field Campaign

The field campaign was carried out in May 2011 in the main tidal channel of the back-barrier basin of the island of Spiekeroog (Figure 2). The campaign was divided into two individual periods, a longer approximately 5 day long station period and a second 3-day transect period. In this paper, we concentrate only on the station period, which is characterized by extensive point measurements at station S in the middle of the channel (see Figure 2). An overview over the entire field campaign with a special focus on the transect period can be found in *Becherer et al.* [2015].

#### 3.2. General Conditions

The general conditions at the study site during the campaign are illustrated in Figure 3. The wind is significantly changing during the observed period, where we distinguish between a situation with moderate winds from the north-west during the first two and a half days ( $P_c$  in Figure 3), followed by a windy period ( $P_w$  in Figure 3), which lasts until the end of the observations (Figure 3a). The second period is characterized by strong winds up to  $10 \text{ m s}^{-1}$  predominately from the West. Note that the wind direction points along the main axis of the channel, which has a west-east orientation at the study site (Figure 2).

The major tidal component in the Wadden Sea is the  $M_2$  semidiurnal tide, which at the study site has an amplitude of approximately 1.3 m for the sea-surface elevation and about  $1 \text{ m s}^{-1}$  for the along-channel velocity (Figure 3b). Nevertheless, it is important to note that there is a diurnal component as well, since we find a periodic difference in the amplitude of two consecutive tidal cycles. The tidal amplitude remains relatively constant over the entire observational period. Although our observations fall in the transition from neap to spring, the difference in amplitude between neap and spring tide is only about 10% [*Becherer et al.*,

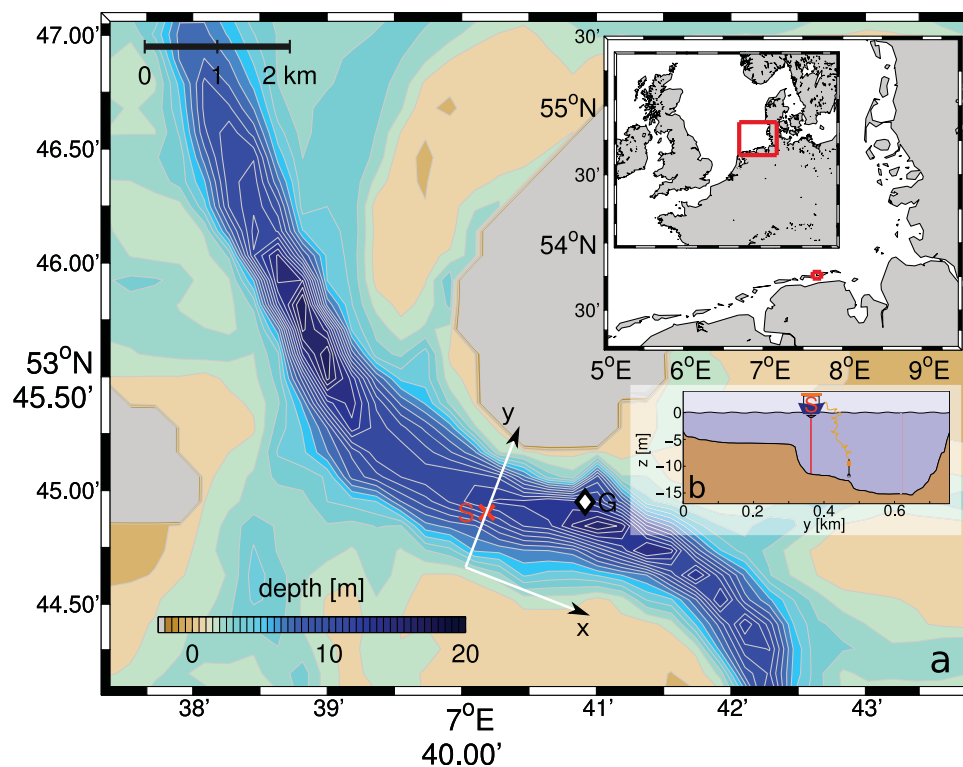


**Figure 2.** Study site. (a) A map of the study site in the tidal inlet, between the islands of Langeoog in the West and Spiekeroog in the East, in the German Wadden Sea. The colored contours display the average water depth. S marks the position of the permanently anchored vessel, R/V Ludwig Prandtl, and G the position of the gauge. (b) A cross section of the channel along the y axis is displayed in the small plot to the right.

2015]. The velocity is out of phase with the sea-surface elevation by approximately  $90^\circ$ , indicating a standing tidal wave. A closer look at the depth-averaged velocity (black line Figure 3b) shows an asymmetry, with a significantly shorter high-water than low-water transition. This asymmetry is due to an  $M_4$  tidal component, which is generated by the characteristic hypsometric distribution of the back-barrier water volume [Dronkers, 1986; Stanev *et al.*, 2003]. This yields a relatively short high-water (HW) and a much longer low-water (LW) slack tide. It is interesting to note that in other parts of the Wadden Sea, depending on the shape of the back-barrier basin, this asymmetry can also be reversed [Dronkers, 1986].

In most estuaries, buoyancy gradients are typically generated by a salinity difference between the open sea and a fresh water source. In the Wadden Sea, however, the situation can be fundamentally different. Here we find a strong horizontal temperature difference, where the North Sea waters are significantly colder than the Wadden Sea waters. Hence, we observe a temperature gradient between high-water and low-water of up to  $4^\circ\text{C}$  (Figure 3c). The salinity difference on the other hand is very small ( $\approx 0.1 \text{ g kg}^{-1}$ ), with larger values during LW than during HW, indicating a slightly more saline Wadden Sea than the open North Sea. However, it is important to note that the effect of salinity on density can almost be neglected. This becomes obvious when we look at the density anomaly in Figure 3d, which nearly perfectly mirrors the temperature evolution (Figure 3c).

Despite an opposing salinity difference, we observe a clear horizontal density gradient, with significantly denser North Sea than Wadden Sea waters. This is expressed as a horizontal buoyancy gradient (black line Figure 3d), which is about  $4 \times 10^{-7} \text{ s}^{-2}$  at the beginning of the observation period, slowly decreasing by a factor of two during the windy period. The horizontal buoyancy gradient is calculated by assuming a predominant balance between along-channel advection and the rate of change in the depth integrated transport equation for the buoyancy (for details on the calculation of the along-channel buoyancy gradient see Becherer *et al.* [2015]). It is important to note that a positive buoyancy gradient corresponds to a *classical* estuary. Therefore, we find the major criteria for the occurrence of estuarine dynamics fulfilled at our study site.

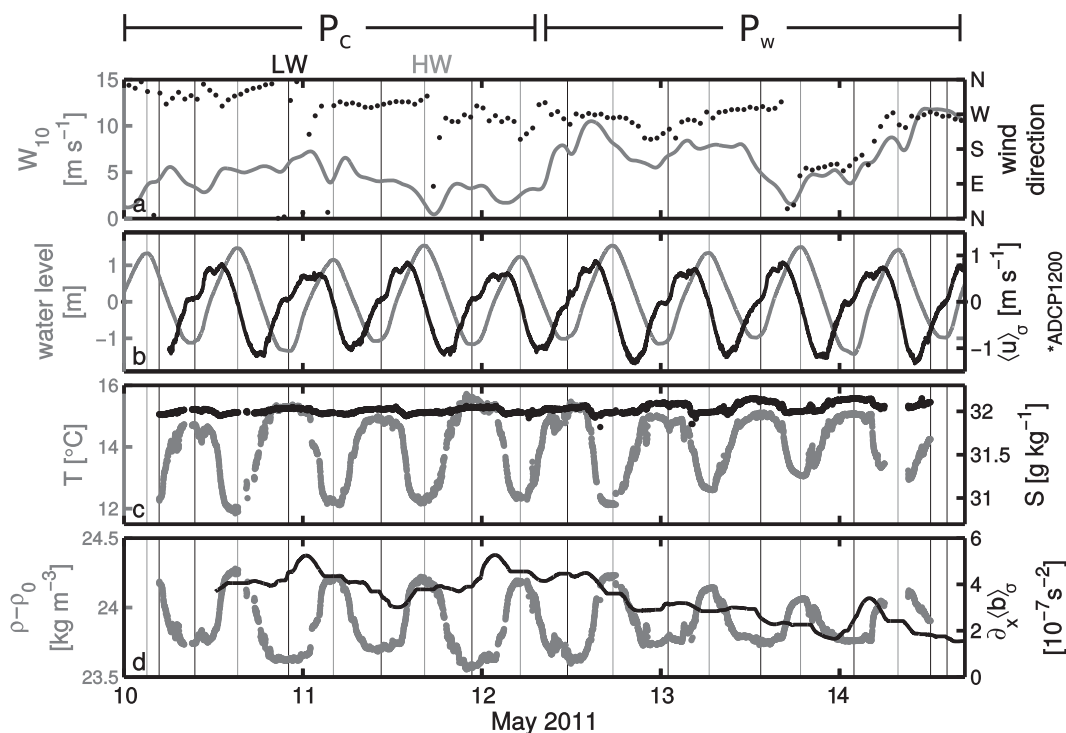


**Figure 3.** Environmental conditions at the study site during the campaign between 10 May and 14 May 2011. (a) Wind speed (gray) and direction (black), (b) water-level (gray) and the depth-mean along-channel velocity (black), (c) depth averaged temperature (gray) and salinity (black), and (d) density (gray) and the along-channel buoyancy gradient (black). The thin vertical lines in each panel mark times of low (black) and high water (gray), respectively. The lines above (Figure 3a) indicate the calm,  $P_c$  and the windy period,  $P_w$ , respectively. Note that the wind direction in Figure 3a is displayed in meteorological convention, where west means from the west. Furthermore, the scales for temperature and salinity in Figure 3c are chosen such that they correspond to comparable changes in density.

### 3.3. Station Measurements

The data set presented here includes 4821 individual microstructure profiles, which corresponds to an average temporal resolution of 77 s over the entire observation period.

Figure 4 gives an overview of the most important quantities measured at station S. The along-channel current velocity is displayed in Figure 4a, where positive (red) values indicate flood tide and negative values (blue) ebb tide. We find tidal currents exceeding  $1 \text{ m s}^{-1}$ , vertically sheared due to bottom friction. HW-slack is significantly shorter than LW-slack, which is due to a hypsometry induced  $M_4$ -overtide (see above). During the first four tidal cycles (low-wind period), we find larger peak ebb than flood velocities, indicating a slight ebb-dominance at the site. Once the westerly winds pick up (second half of the observation period), the situation changes and soon we find stronger flood than ebb currents. It is also interesting to note that in the second period the flood currents appear to be sheared more strongly in the vertical than for ebb tide. This is most likely due to the additional shear originating from the wind stress (wind straining). Due to higher waves during the second part of the campaign, ship movement and air bubble entrainment resulted in an increased number of corrupted velocity records from the ADCP (white shading Figure 4a).

Figures 4b and 4c show the vertical distribution of temperature and salinity, respectively. The temperature is increasing toward low water and decreasing toward high-water slack, indicating significantly warmer Wadden Sea than North Sea waters. Instead of a smooth transition, we can observe a rather sharp front passing by around peak tidal currents. The salinity differences are very small (Figure 4c), less than  $0.1 \text{ g kg}^{-1}$  at the beginning of the observations, slightly increasing toward a maximum HW-LW-difference of  $0.15 \text{ g kg}^{-1}$  at the end.

The observations were conducted at the end of an extraordinarily warm low-wind period lasting for almost two months, which may explain the observed characteristics. Due to the strong solar heating during spring the shallow Wadden Sea became significantly warmer than the deeper North Sea, resulting in a strong horizontal temperature gradient (differential heating). During our observations, the wind increased, causing

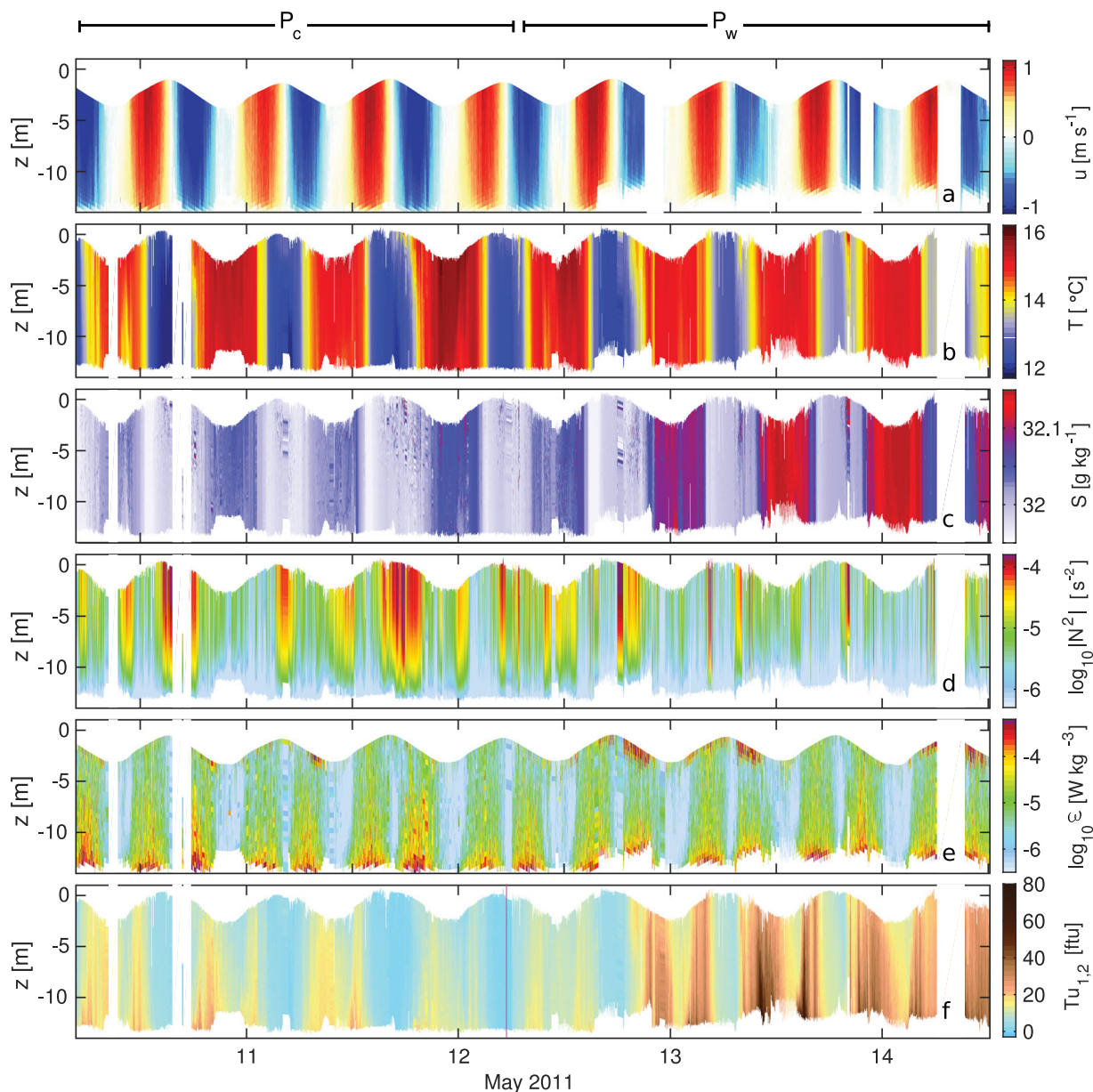


**Figure 4.** Station measurements from the R/V Prandtl. (a) Along-channel velocity, (b) temperature, (c) salinity, (d) buoyancy frequency, (e) dissipation rate of turbulent kinetic energy, and (f) turbidity. The magenta line in Figure 4f indicates sensitivity change of the turbidity sensor. The lines above (Figure 4a) indicate the calm,  $P_c$  and the windy period,  $P_w$ , respectively.

increased evaporation, which is cooling down the shallow Wadden Sea and at the same time increasing salinity. Therefore, we find a slowly decreasing horizontal density gradient toward the end of our observation period (compare Figures 4b, 4c, and 3d).

In the vertical, the water column is well mixed with very small values of the buoyancy frequency most of the time (Figure 4d). Only at slack tides and at early flood and ebb significant stratification can be found, with values reaching  $N^2 = 10^{-4} \text{ s}^{-2}$ . In general, we observe a slight trend of decreasing stratification toward the end of the observation period. This could be due to generally weaker density gradients in the horizontal and enhanced mixing caused by stronger winds.

The turbulence level is high most of the time with dissipation rates of turbulent kinetic energy,  $\varepsilon$ , reaching  $10^{-4} \text{ W kg}^{-1}$  throughout the entire water column (Figure 4e). The largest values of  $\varepsilon$  can be found at peak tidal currents close to the bottom, indicating that the major source of turbulence in the system is bottom

friction caused by tidal currents. We observe a slight ebb-flood asymmetry of the dissipation rates, where stronger turbulence seems to be generated close to the bottom during ebb than during flood tide. This is consistent with the slight ebb-dominance at our site, which we already mentioned above.

The turbidity of the water column is displayed in Figure 4f, where we find increased values around but not exactly at low-water slack. In general, we observe a slowly decreasing turbidity during the first quiescent period and finally strongly elevated turbidity values in the second strong-wind period. At times of strong turbulence, we find a vertically homogeneous turbidity distribution whereas during slack tides we observe a clear stratification, with increasing turbidity values toward the bottom.

#### 4. Exchange Flow

The major aim of this study is to quantify tidal SPM transport and its relation to estuarine circulation (landward residual flow near the bottom and seaward residual flow near the surface). It is commonly assumed that the interaction of a tidally averaged SPM profile (higher concentrations near the bed than near the surface) with estuarine circulation results in a net landward SPM transport.

Some observational evidence for the existence of estuarine circulation in the Wadden Sea has been presented by *Flöser et al.* [2013]. These authors use, besides other longer time series, also parts of the ADCP data presented here. In principle, we follow a similar approach as *Flöser et al.* [2013] to quantify estuarine circulation. However, here we apply a slightly more sophisticated technique to close existing data gaps, which is necessary to get a full picture of the exchange flow over the entire length of the campaign and to be able to perform correlations between the velocity and sediment measurements (see section 2).

##### 4.1. Tidal Averaging Method

The flow characteristics of estuarine circulation are difficult to measure in energetic tidal systems like the Wadden Sea. This is because the residual exchange flow is expected to be at least 1 order of magnitude smaller than the tidal currents in such systems. Therefore, it is necessary to treat the velocity measurement carefully in order to investigate this secondary effect.

To quantify the residual estuarine exchange flow based on our velocity measurement it is necessary to apply an averaging procedure based on the following three steps:

1. All available data are interpolated on a grid of 20 equidistant vertical layers ( $\sigma$ -layers see section 2.1) that change their height due to the sea-surface elevation.
2. Potential data gaps are closed by interpolation along the  $\sigma$ -layers.
3. By using a weighted averaging procedure given in equation (5), the data are tidally averaged along the  $\sigma$ -layers.

Any error related to the interpolation along  $\sigma$ -layers is believed to be rather small, since significant data gaps only occur at the very end of the observation period. In this context it is important to note that we exclude the very last 12 h of the observations from the flux calculations, where we find a very long data gap (see Figure 4).

##### 4.2. Along-Channel Exchange Flow

Figure 5a shows the along-channel velocity component interpolated on the  $\sigma$ -grid, where all the data gaps caused by measurement errors during the strong-wind period have been closed by interpolation. Note that the first four  $\sigma$ -layers close to the surface cannot be filled with data, since the ADCP is mounted at a depth of 1.4 m and has itself a blanking distance of about a meter. Therefore, the first 2.5 m of the water column cannot be measured.

If we apply (5) to the along-channel velocities, we obtain the tidally averaged along-channel flow,  $\langle u \rangle_\tau$ , which is displayed in Figure 5b. Until 12 May in the quiescent period (less wind), the tidally averaged along-channel velocity shows a characteristic exchange flow. Close to the bottom the water moves into the Wadden Sea (landward), whereas further up in the water column it moves seaward. This is in good agreement with the theory of estuarine circulation.

However, during 12 May, the situation changes dramatically. The tidal mean currents throughout the entire water column become strongly positive (landward directed), which is most likely associated with the

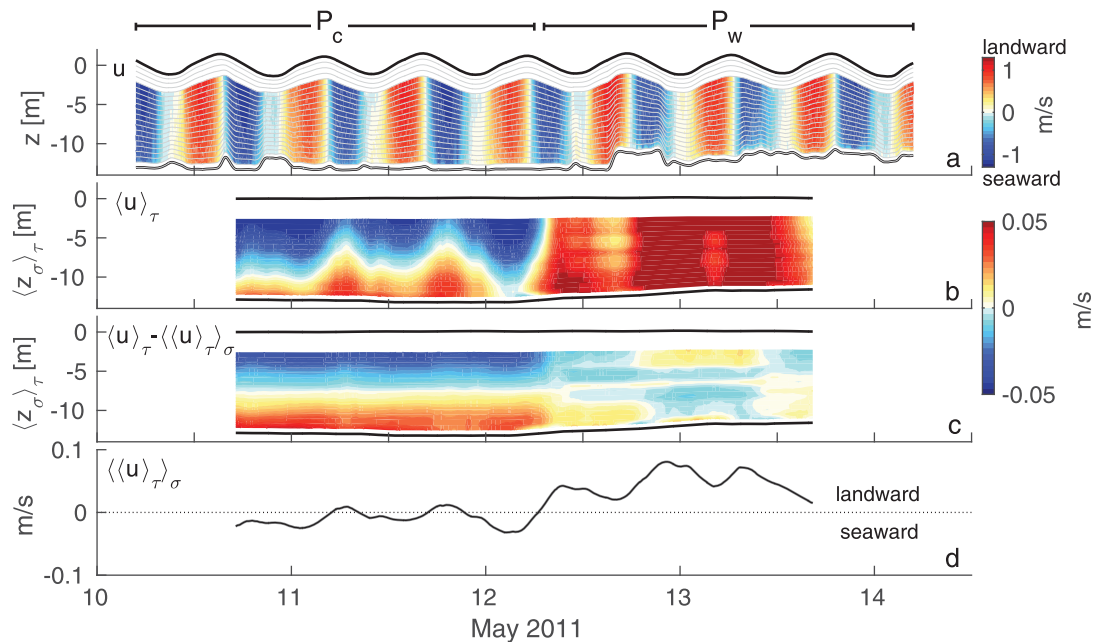


**Figure 5.** Along-channel velocity. (a) Along-channel velocity,  $u$ , interpolated on the  $\sigma$ -grid, (b) tidally averaged  $u$ , (c) depth-anomaly of the tidally averaged  $u$ , and (d) depth-mean of the tidally averaged  $u$ . The light gray lines in Figure 5a show the height of the  $\sigma$ -layers and the black lines illustrate the height of the bottom and the sea-surface elevation, respectively. The black lines in Figures 5b and 5c display the tidally averaged height of the bottom and surface, respectively. The lines above (Figure 5a) indicate the calm,  $P_c$  and the windy period,  $P_w$ , respectively.

increasing westerly winds. The additional eastward directed wind forcing yields an up-estuary (landward) directed flow. The signature of the estuarine exchange flow is wiped out almost entirely.

The net barotropic flow component is illustrated in Figure 5d, which is simply the depth-mean of the tidally averaged along-channel velocity. At the first quiescent period we find a small ebb-dominance, but once the winds increase, the system changes toward a strong flood-dominance, with depth-mean residual currents of more than  $5 \text{ cm s}^{-1}$ .

If we subtract the barotropic component from the tidally averaged velocity, we obtain the pure exchange flow (Figure 5c). The estuarine circulation signature of the flow during the first half of the observation period becomes even more pronounced. As soon as the westerly winds pick up speed the exchange signal first becomes weaker and finally even slightly reverses.

There are three different mechanisms associated with the strong westerly wind that potentially reduce the strength of the estuarine exchange flow:

1. The shear stress induced by the landward-directed winds is in principle oriented such that it opposes the classical estuarine circulation [see Purkiani *et al.*, 2016].
2. The additional turbulence associated with the waves and the sea-surface shear stress increase vertical mixing and thus has the tendency to suppress the baroclinic exchange flow.
3. The increased evaporation associated with the stronger winds yield an increase in density in the Wadden Sea and thus a reduced horizontal density gradient (review discussion section 3.2), which is in fact the primary driver of estuarine exchange flow.

It is difficult to discriminate, which of these processes is of greater importance. However, we can say that the combination of all three mechanism leads to a strong reduction and finally even to a reversal of the exchange flow.

Note that the barotropic flow component is affected by the fact that we are missing the upper 2.5 m of the water column. If we would have included this upper part of the water column in our calculations, we would have expected to see a more elevated ebb-dominance during calm conditions, but also an even stronger flood directed wind driven flow during  $P_w$ . This change in barotropic flow would also affect the exchange flow component, where we would see the zero-crossing of the velocity to be further up in the

water column. Those differences however would not substantially change the qualitative statements above.

### 4.3. Across-Channel Exchange Flow

When we look at the  $y$ -component of the velocity (Figure 6a) we find it to be about 1 order of magnitude smaller than the along-channel component. However, the tidal mean lateral exchange flow is of the same strength as the along-channel exchange (Figure 6b). This is primarily due to a pronounced clockwise (looking up-estuary) lateral circulation during end of flood and a missing counter circulation during ebb tide. This phenomenon was first described and analyzed in detail by *Becherer et al.* [2015]. The authors find the asymmetric lateral circulation to be due to a systematic interplay between the baroclinic pressure gradient and the curvature of the channel, where the lateral buoyancy gradient is oriented in such a way that it enhances curvature induced lateral circulation during flood and compensates it during ebb. The authors furthermore concluded that this systematic interplay may be a characteristic feature of curved channels in weakly stratified estuarine systems like the Wadden Sea.

The barotropic component of the flow is very small, most of the time less than  $1 \text{ cm s}^{-1}$ . This is not very surprising given the fact that the coordinate system is rotated such that the  $M_2$ -tidal component is minimized. The remaining net barotropic flow seems to be due to the strong oscillatory barotropic current at the end of ebb tide. This feature, already observed by *Becherer et al.* [2015], is coherent over the entire width of the channel, but not yet well understood. It is potentially due to the relaxation of a lateral barotropic pressure gradient, which is associated with the curved ebb-flow.

If we look at the pure exchange circulation of the mean lateral flow, we find it to be largest at the beginning of the observation period (see Figure 6c). During the strong-wind period, it decreases by about a factor of 2. This is in contrast to the along-channel exchange, which vanishes completely. The lateral exchange flow is influenced by the same suppressing mechanisms as the along-channel flow, except for the direct shear stress of the westerly winds. This suggests that the directed shear stress accounts approximately to the same amount of suppression of estuarine exchange flow as the two other processes, mixing and gradient reduction, combined.

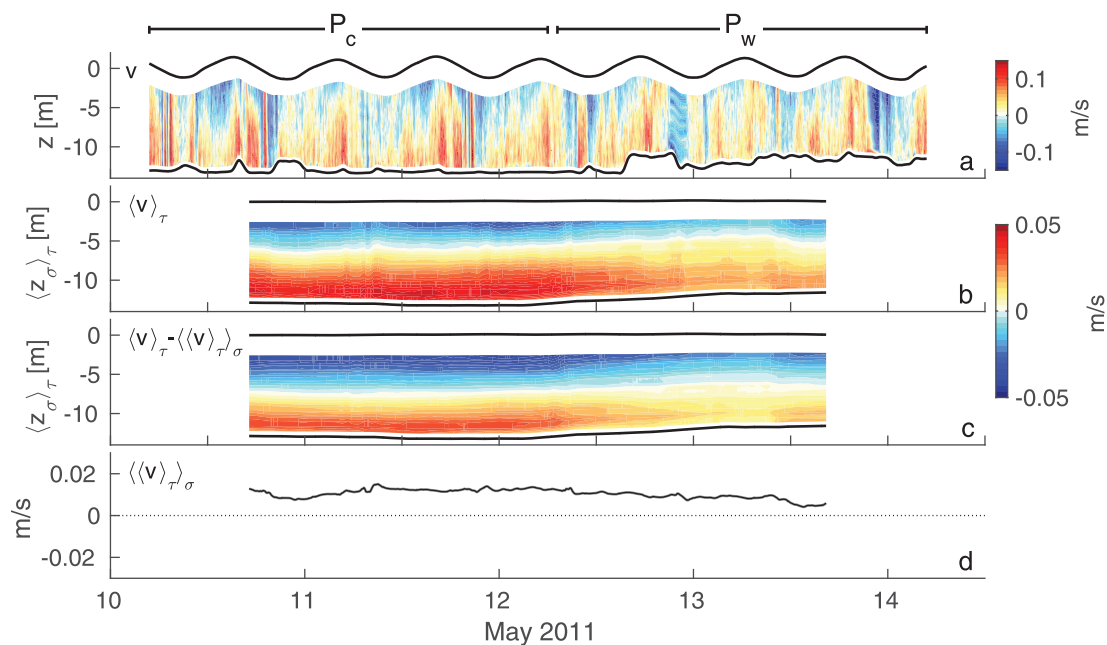


**Figure 6.** Across-channel velocity. (a) Across-channel velocity,  $v$ , interpolated on the  $\sigma$ -grid, (b) tidally averaged  $v$ , (c) depth-anomaly of the tidally averaged  $v$ , and (d) depth-mean of the tidally averaged  $v$ . The black lines in Figure 6a show the height of the bottom and the sea-surface elevation, respectively. The black lines in Figures 6b and 6c display the tidally averaged height of the bottom and surface, respectively. The lines above (Figure 6a) indicate the calm,  $P_c$  and the windy period,  $P_w$ , respectively.

## 5. Sediment Dynamics

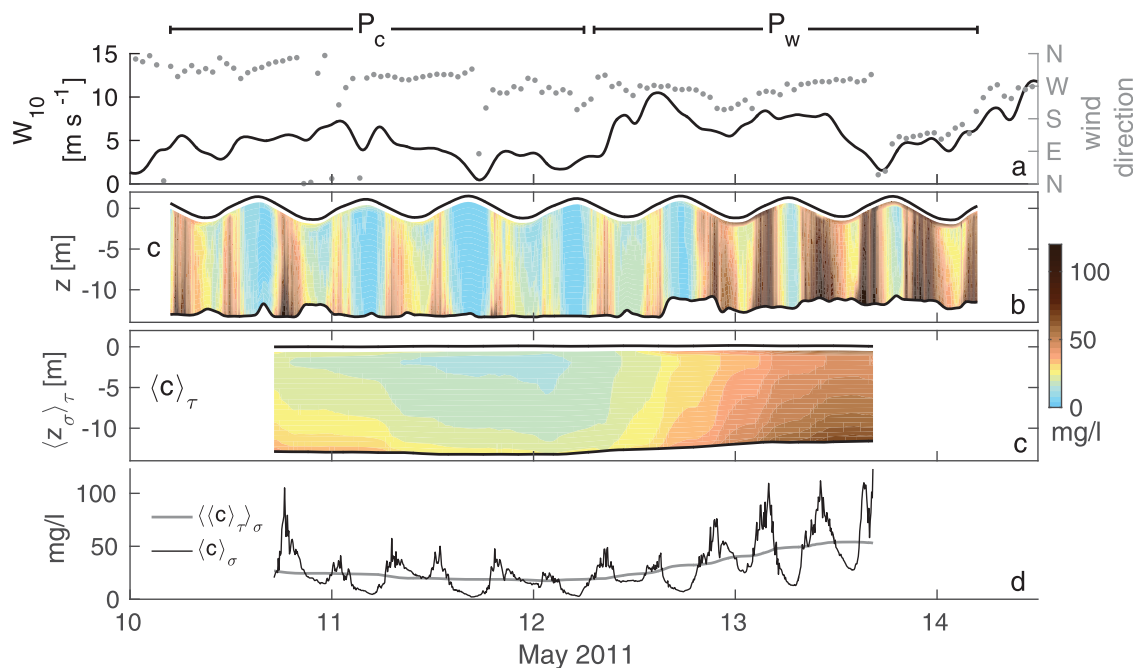
### 5.1. Sediment Concentration

Figure 7a shows turbidity data transformed into sediment concentrations with the help of the calibration procedure described in section 2.5. In analogy to the ADCP data, we interpolated the SPM-data on the  $\sigma$ -grid to be able to perform tidal averages and furthermore to correlate velocities and sediment concentration in order to calculate sediment fluxes.

Figure 7 illustrates that there is a large variability of sediment concentration in the water column. We find a clear tidal variability (Figure 7), where largest concentrations occur shortly before and after LW-slack. Toward HW-slack, on the other hand, we find relatively low concentrations. On top of this intertidal variability, we observe a general trend, of slowly decreasing concentration during the quiescent period, followed by a rapid increase of suspended sediment during the strong-wind period (Figure 7).

An explanation for the short term variability must be slightly more complicated. If the tidal currents would significantly contribute to the erosion of sediment, one would expect large sediment concentrations to be associated with strong tidal currents. We have seen in section 3.2 that the tidal peak currents are shifted toward HW-slack, which is due to the hypsometry of the back-barrier basin [Dronkers, 1986; Stanev et al., 2003]. However, largest sediment concentrations are found around LW-slack. This suggests that the tidal currents are not the major eroding agent of sediment observed at our site. Instead, wave erosion on the intertidal flats must be the major sediment source. Since the bed at our observation site (middle of the tidal channel) is too deep to be substantially affected by wave stresses, we conclude that most of the sediment observed at our site is not due to local erosion but advection from shallower regions in the back-barrier basin. This also explains why we observe the peak concentrations short before and after LW-slack. At the end of ebb tide the water which remained longest on the flats passes our site, carrying large sediment loads. During LW-slack turbulence goes down and the suspended sediment starts to sink. Once the tidal currents pick up speed at the beginning of flood, the fine sediments can be easily resuspended. This explains as well the fact that the ebb SPM peak is much wider than the relatively short early-flood peak (Figures 7c and 7d).

Such a situation of nonlocally eroded SPM is potentially typical for deeper channels associated with large intertidal flats, where the channels provide a transportation network to distribute the sediments that are



**Figure 7.** SPM concentration. (a) Wind speed (black) and direction (gray), (b) SPM concentration interpolated on the  $\sigma$ -grid, (c) tidally averaged SPM concentrations, and (d) vertical mean of the SPM concentration (black) and its tidal average (gray). The thick black lines in Figures 7b and 7c indicate the height of the surface and bottom, respectively. The lines above (Figure 7a) indicate the calm,  $P_c$  and the windy period,  $P_w$ , respectively.

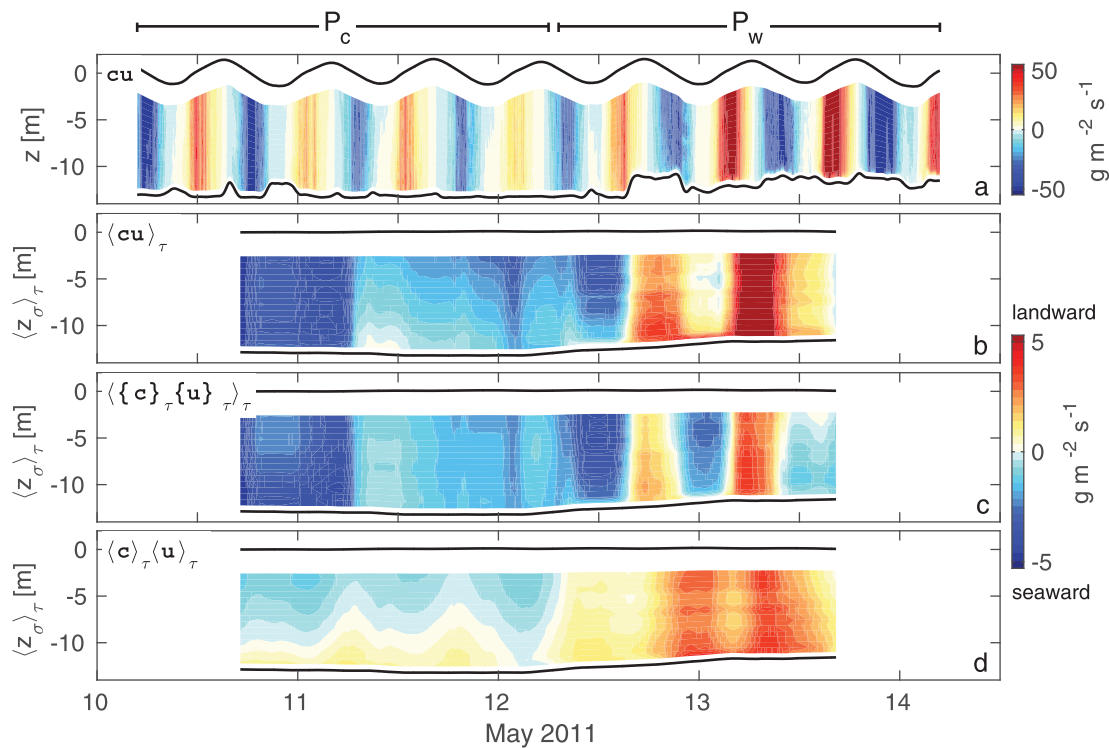


**Figure 8.** Along-channel sediment flux. (a) Product between the sediment concentration  $c$  and the along-channel velocity  $u$ , both interpolated on the  $\sigma$ -grid, (b) tidal average of the sediment flux, (c) tidal pumping contribution, and (d) advective-flux contribution. Positive values correspond to landward and negative values to seaward transport, respectively. Thick lines indicate the height of the surface and bottom, respectively. The lines above (Figure 8a) mark the calm,  $P_c$  and the windy period,  $P_w$ , respectively.

eroded on the flats. The role of the tidal currents in terms of the sediment dynamics is thus not primarily erosion, but rather advective transport and turbulence generation to prevent the sediment from sinking. Since our observations are taken at a single point in the tidal channel, it is possible to cover only a fraction of the total complexity of the sediment dynamics in the intertidal basin.

## 5.2. Along-Channel Sediment Fluxes

To study how the tidal currents drive along-channel sediment transport at our observation site, we multiply the sediment concentrations,  $c$ , and the along-channel velocities,  $u$ , after interpolation on the same  $\sigma$ -grid (Figure 8a). We observe a strong periodicity with peak fluxes of about  $50 \text{ g m}^{-2} \text{ s}^{-1}$  into the Wadden Sea (landward) during flood and in the opposite direction during ebb. The amplitude of the flux follows at first order the mean sediment concentration, yielding a relatively small amplitude during the quiescent and a large amplitude during the strong-wind period.

The tidally averaged along-channel flux is primarily seaward (blue) during the first quiescent period (Figure 8b). Only on 11 May, we find some small landward-directed (red) counter flux close to the bottom. During the strong-wind period, the tidal mean flux is undulating between a small seaward and a stronger landward flux.

Following the decomposition described in section 2.3, it is possible to divide the tidally averaged sediment flux into a advective contribution,  $\langle c \rangle_{\tau} \langle u \rangle_{\tau}$  (Figure 8d), and a tidal pumping contribution,  $\langle \{c\}_{\tau} \{u\}_{\tau} \rangle_{\tau}$  (Figure 8c). If we compare the tidal pumping contribution to the tidally averaged total flux (Figures 8b and 8c), both distributions appear very similar. The major differences are the missing counter flux on 11 May and that the undulating behavior during the windy period seems to be shifted much further toward the seaward direction for the tidal pumping flux compared to the total flux.

The advective flux (Figure 8d) accounts for the difference between  $\langle \{c\}_{\tau} \{u\}_{\tau} \rangle_{\tau}$  and  $\langle cu \rangle_{\tau}$ . During the quiescent period we observe a well-developed vertical exchange flux, where the sediment in the lower water

column is transported landward and in the upper water column seaward, reflecting the signature of estuarine circulation. During the second windy period, we find a strong landward advective flux throughout the entire water column due to the barotropic current induced by the westerly winds.

Figure 9 illustrates the vertically integrated mean flux. By vertical integration, it is possible to split the advective flux even further, into a barotropic component,  $F_{\text{bfr}}^x$ , and another component purely due to estuarine circulation,  $F_{\text{exf}}^x$  (for details see section 2.3). During the quiescent period ( $P_c$ ) the total sediment flux (black) approximately follows the tidal pumping contribution (blue). The depth-integrated advective contribution (red) is off minor importance and itself almost entirely dominated by the barotropic component (purple). The exchange flow component (yellow) is positive (landward) throughout the entire calm period, but, regarding its magnitude, very small compared to all the other terms involved. Note that  $F_{\text{exf}}^x$  was even multiplied by a factor of 10 to make it visible in Figure 9, which illustrates that its contribution to the total sediment flux is practically negligible.

If we look at the second windy period ( $P_w$ ) the situation changes significantly. The advective flux (red) becomes strongly positive, and it is entirely dominated by its barotropic component (purple). The exchange flow component (yellow) vanishes completely. The strong advective flux causes the entire depth integrated sediment flux to be landward directed. But also the tidal pumping flux (blue) remains important. During the windy period, it starts to undulate around negative values with a  $M_2$ -tidal period. This strange undulating behavior is due to our tidal averaging procedure. The sediment concentrations increase dramatically once the wind becomes stronger during the ebb tide in the evening of 12 May (Figure 7c). The moving average fully contains this particular ebb tide at mid-day of 12 May, where we find strong negative values of  $F_{\text{tpf}}^x$  (blue line Figure 9). When we move further, we start to include the consecutive flood tide, leading even to positive values and so on.

In summary, we find the calm period to be dominated by a seaward-directed tidal pumping flux and the windy period by a landward-directed barotropic flux, which becomes even more obvious by removing the superimposed undulations by low-pass filtering (see thick solid lines in Figure 12). If we would be able to furthermore include the upper 2.5 m into our calculations, this general trend would be more pronounced, with a stronger ebb-oriented flux during calm conditions and an even stronger landward oriented flux during the windy period. The contribution of the exchange flow component to the depth integrated sediment flux is landward directed but very small during the calm period and completely negligible during the windy period. The signature of the exchange flow is clearly visible in the vertically resolved illustration of the advective flux (Figure 8d). However, its vertically integrated contribution is very small (yellow line Figure 9).

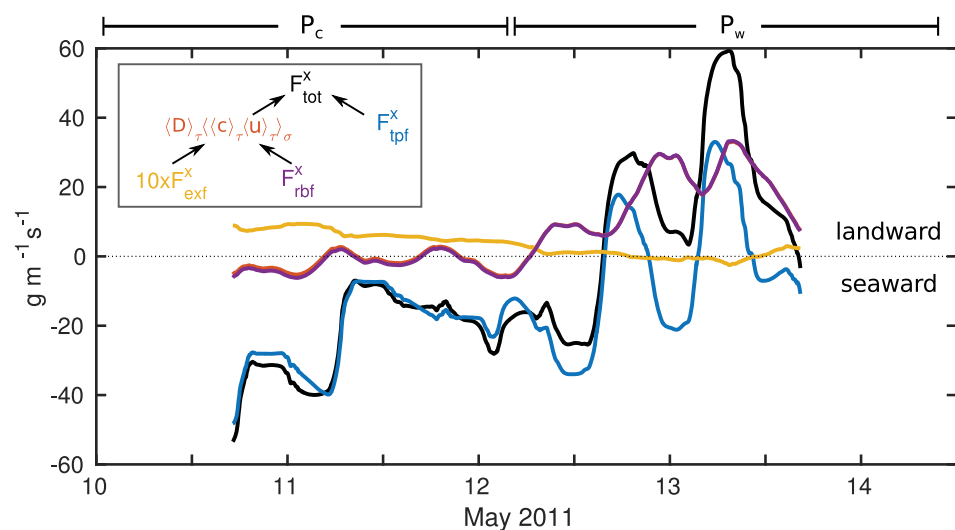


**Figure 9.** Vertically integrated along-channel sediment flux (see equation (15)). The total vertically integrated flux (black) consists of a tidal pumping contribution (blue) and a advective flux (red), which itself consists of a barotropic component (purple) and an exchange flow component (yellow). Note that  $F_{\text{exf}}^x$  was multiplied by a factor of 10 to make it visible in the given scale. The lines above (Figure 9a) indicate the calm,  $P_c$  and the windy period,  $P_w$  respectively.

The sediment is vertically well mixed most of the time, hence a landward-directed flux at the bottom is almost entirely compensated by a corresponding seaward flux at the surface.

### 5.3. Across-Channel Dynamics

The across-channel sediment fluxes (Figure 10a) are generally weaker than the along-channel fluxes, in agreement with the weaker lateral than longitudinal current velocities. However, it is possible to identify some characteristic patterns. During most of flood and the beginning of each ebb tide we observe an exchange flux, where the sediment is transported northward at the bottom and southward at the surface. This exchange flux is strongest at the beginning of flood, where we find large sediment concentrations combined with a significant lateral exchange flow (compare Figures 6a, 7a, and 10a). Another recurring feature is a strong southward flux throughout the entire water column at the end of ebb tide, which is always interrupted by a similar strong flux in the opposite direction. This short barotropic flux oscillation is obviously associated with the corresponding lateral flow oscillation at the end of ebb tide (Figure 6a), which might be related to the relaxation of a lateral sea-surface gradient initially caused by the curved ebb currents.

The net sediment flux in the lateral direction (Figure 10b) is characterized by a persistent exchange flux, where sediment is transported northward (red) at the bottom and southward (blue) at the surface, respectively. The advective component (Figure 10d) looks very similar like the distribution of the total flux,  $\langle cv \rangle_\tau$ , showing an even more pronounced vertical exchange. The tidal pumping component,  $\langle \{c\}_\tau \{v\}_\tau \rangle_\tau$  (Figure 10c), is negative (southward) throughout the water column, but significantly smaller in magnitude than  $\langle c \rangle_\tau \langle v \rangle_\tau$ .

In the vertically integrated lateral sediment flux (Figure 11), the exchange flow component (yellow) becomes less dominant than in the vertically resolved picture (Figure 10). The total vertically integrated lateral sediment flux (black) is northward directed (positive) during the entire observation period. In contrast to the along-channel flux, the lateral advective flux (red) is not entirely dominated by its barotropic component (purple), but also to a large fraction by the exchange flow (yellow), particularly during the quiescent

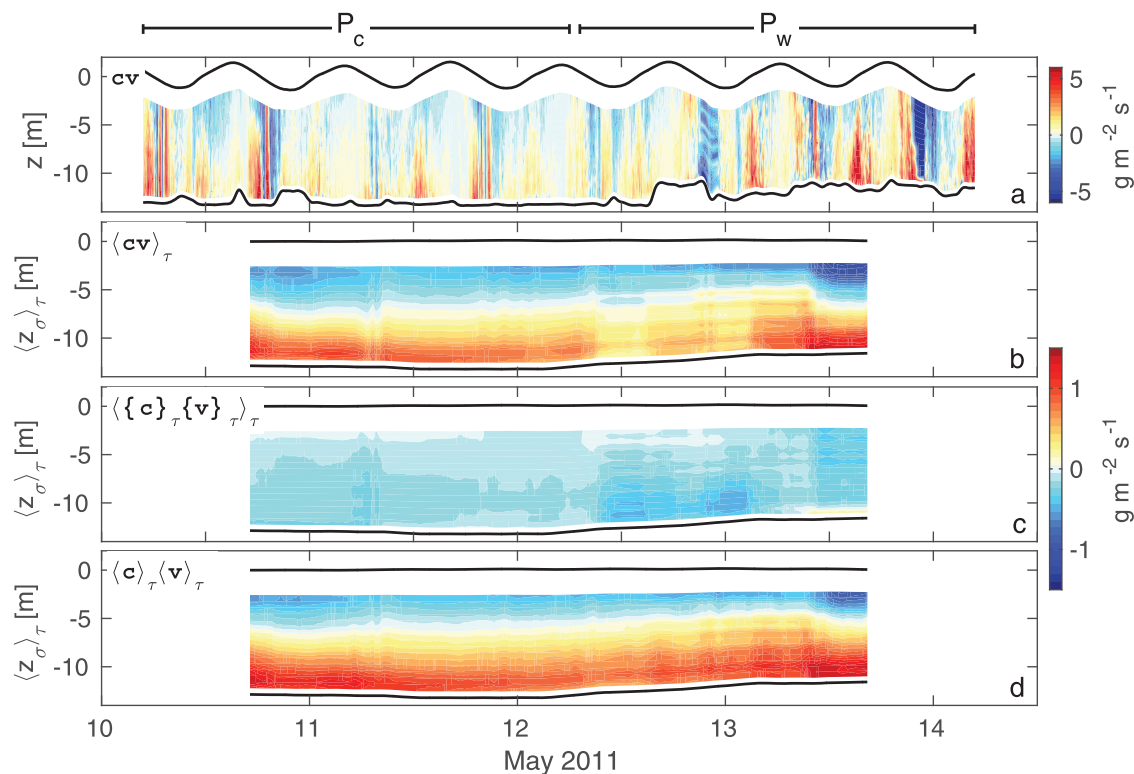


**Figure 10.** Cross-channel sediment flux. (a) Product between the sediment concentration  $c$  and the cross-channel velocity  $v$ , both interpolated on the  $\sigma$ -grid, (b) tidal average of the sediment flux, (c) tidal pumping contribution, and (d) advective-flux contribution. Positive values correspond to northward and negative values to southward transport, respectively. Thick lines indicate the height of the surface and bottom, respectively. The lines above (Figure 10a) mark the calm,  $P_c$  and the windy period,  $P_w$ , respectively.

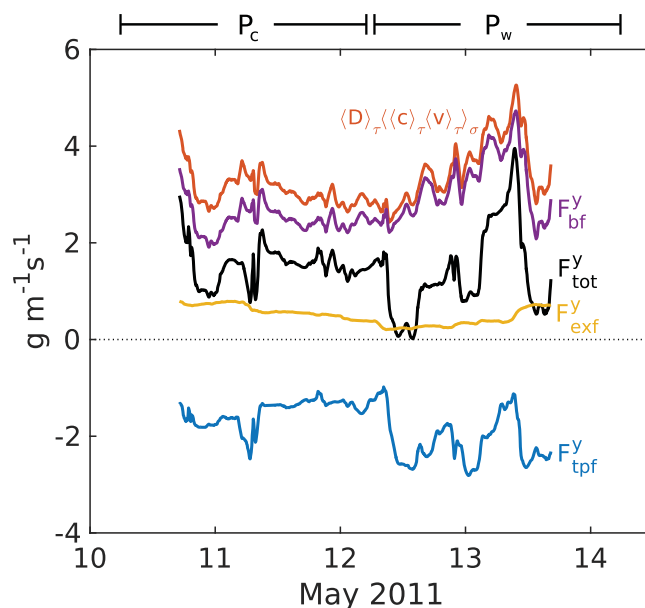


**Figure 11.** Vertically integrated across-channel sediment flux. The total vertically integrated flux (black) consists of a tidal pumping contribution (blue) and an advective flux (red), which itself consists of a barotropic component (purple), and an exchange flow component (yellow). The lines above (Figure 11a) indicate the calm,  $P_c$  and the windy period,  $P_w$ , respectively. Note that here in contrast to Figure 9 the exchange flow component,  $F_{exf}^y$ , is not multiplied by 10, but shown in the same scale as the other terms.

period. The vertically integrated tidal pumping component is negative (southward) during the entire observation period. In general, we find the tidal pumping flux (blue) and the barotropic flux (purple) approximately compensating each other most of the time. Both gain slightly in magnitude during the strong-wind period, however still reversing each other.

The major reason for the persistent lateral sediment flux in northward direction seems to be the exchange flow component (yellow). Interestingly,  $F_{exf}^y$  is surprisingly constant during the entire observation period. The weaker lateral circulation during the windy period (see discussion above) is compensated by increased sediment concentrations. Therefore, the across-channel sediment flux due to residual lateral circulation, toward the more ebb dominated side of the channel, appears to be a more robust feature than the highly wind dependent along-channel transport.

#### 5.4. Comparison of Methods

Since our procedure to decompose the sediment flux slightly deviates from the more commonly used method that was first introduced by Geyer *et al.* [2001], it seems worthwhile to briefly compare both methods. Geyer *et al.* [2001] suggested to calculate the advective flux based on the product of the low-pass filtered velocity and the low-pass filtered sediment concentration. The low-pass filtered correlation of the high frequency part of both signals ( $u'$  and  $c'$ ) provides the tidal pumping flux (for details on the decomposition see e.g., Geyer *et al.* [2001] and Sommerfield and Wong [2011]).

Figure 12 compares the net along-channel sediment flux based on the method proposed in this paper in section 2.3 (solid lines) to the method introduced by Geyer *et al.* [2001] (dashed lines). The results of our method (thin solid lines) have been low-pass filtered (36 h, thick solid lines) to allow for a better comparison. Correspondingly, we used a 36 h low-pass filter for the method by Geyer *et al.* [2001], which is in agreement with earlier studies [e.g. Sommerfield and Wong, 2011; McSweeney *et al.*, 2016]. The estimates for the advective (red), the tidal pumping (blue), and the total flux (black) of our method (solid lines) agree well with the procedure proposed by Geyer *et al.* [2001] (dashed lines). Both methods are able to reproduce the general trend of a decreasing seaward-directed tidal pumping flux and an increasing landward-directed advective flux, causing the total flux to change sign during the transition from the calm to the windy period.

Although both procedures give comparable results, we note significant differences. The major drawback of the methods proposed by Geyer *et al.* [2001] is that it does not provide a closed balance, which means that the sum of the advective and the tidal pumping flux (dashed gray line in Figure 12) does not exactly correspond to the total sediment flux (dashed black line). The discrepancy is due to cross-correlation terms between the mean velocity and the fluctuating sediment concentration and vice versa. Because of their difficult interpretation, those terms have been usually neglected by former studies, although they can be significant in situations where the mean state of the system changes rapidly. The method proposed here in section 2.3 does not have this issue, since it is constructed in such way that it yields a perfectly closed balance, where the sum of all terms exactly corresponds to the total sediment flux. This exact balance allows

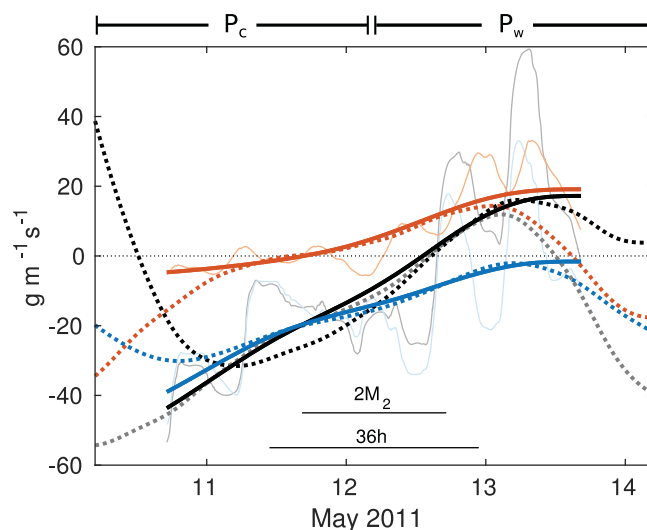


**Figure 12.** Comparison of different decompositions for the mean along-channel sediment flux. The thin black, red, and blue line show the total, advective, and tidal pumping flux, respectively, based on (15) (same as in Figure 9). The thick solid lines are low-pass filtered (36 h) version of the thin lines using the same color-coding. The dashed lines show the corresponding terms based on the more commonly used method by Geyer *et al.* [2001]. The dashed gray line illustrates the sum of the dashed red and blue line.

for a meaningful further decomposition of the advective flux into an exchange flow and a barotropic component.

The downside of our method is related to the box-average, which can result in an undulating behavior caused by a sudden increase in amplitude of the tidally oscillating sediment flux. By sudden, we mean on time scales much smaller than our filter length. The gain in amplitude is due to rapidly increasing resuspension of sediment associated with the onset of waves during the windy period. However, also the low-pass filter method of Geyer *et al.* [2001] can yield problems, especially when the filter width is of a similar order as the length of the analyzed time series. In our case, we find for instance an unreasonable behavior of the low-pass filtered signals at both edges of the time series (dashed lines in Figure 12).

Both methods have their advantages and drawbacks. The choice of the appropriate method therefore depends on the available data set and the particular analyzing purpose.

## 6. Discussion and Conclusions

In this paper, we used a flux-averaging procedure along  $\sigma$ -layers to calculate the residual circulation in the middle of a tidal channel in the Wadden Sea. We found a residual exchange circulation, directed landward at the bottom and seaward at the surface. Despite the fact that many studies postulated the existence of estuarine circulation in the Wadden Sea [e.g., Burchard *et al.*, 2008; Becherer *et al.*, 2011; Flöser *et al.*, 2011; Becherer, 2014], our data show the first direct observations. However, we only observed estuarine circulation during a calm period with moderate wind conditions. During larger wind speeds in up-channel direction, we find estuarine circulation to vanish or even reverse, which is clearly associated with additional vertical shear due to surface stress. We therefore find the wind to be an important agent in controlling the strength and direction of the vertical exchange circulation, which is in agreement with a recent model study by Purkiani *et al.* [2016].

Besides the wind, there are many different processes involved that can drive estuarine circulation in such highly energetic systems. Although we did not try to discriminate the individual processes, earlier studies [e.g., Burchard and Hetland, 2010; Becherer, 2014; Becherer *et al.*, 2015; Schulz *et al.*, 2015] suggest an elevated importance of tidal current asymmetries over classical gravitational circulation. These asymmetries can be caused for instance by tidal straining [Burchard and Hetland, 2010; Becherer *et al.*, 2011] or by lateral rectification of the tidal currents associated with asymmetric secondary circulation [Lerczak and Geyer, 2004; Becherer *et al.*, 2015; Schulz *et al.*, 2015].

The major aim of this study is to investigate the relative importance of the different drivers of sediment transport in shallow and highly energetic systems like the Wadden Sea. Like earlier studies [Geyer *et al.*, 2001; Scully and Friedrichs, 2007; Burchard *et al.*, 2013; McSweeney *et al.*, 2016], we distinguish between an advective flux and a tidal pumping flux, where the first is due to residual currents and the second due to the intertidal correlation between sediment concentrations and current velocities. The method presented here (section 2.3) however allows for a further decomposition of the advective flux into an exchange flow component and another component that is due to residual barotropic currents. The latter accounts for

effects of residual barotropic flows caused by ebb-dominance or flood-dominance, wind stress, and/or river runoff.

At our observation site in the middle of the channel, the SPM concentrations are highly variable in time but vertically usually well mixed. Interestingly, largest SPM concentrations do not occur during peak tidal currents. Instead, we find an ebb and a corresponding flood peak in SPM concentration shifted toward LW-slack. This observation indicates that the sediment is not primarily locally eroded due to tidal currents, but rather due to wind waves at the surrounding intertidal flats. Hence, the tidal channels in the Wadden Sea seem not to be the primary source or sink for sediment, but rather work as a distribution network for sediment eroded and deposited at the intertidal flats.

The net sediment flux at our channel site is dominated by tidal pumping, resulting in a seaward sediment transport during the calm period. However, once the along-channel winds increase, the barotropic component becomes increasingly important, yielding a substantial eastward (landward) sediment transport, probably across the watershed toward the next tidal basin. The exchange flow component of the sediment flux is always landward directed, but generally much weaker than the two other contributors. These findings are in good agreement with predictions based on an idealized model by *Burchard et al.* [2013].

The fact that the exchange flow component of the sediment flux is relatively weak, implies a minor importance of estuarine circulation to the net sediment transport in the Wadden Sea. However, this is only partially true, since many of the processes that are involved in the generation of the residual estuarine circulation may also significantly contribute to tidal pumping. As pointed out above, estuarine circulation in well-mixed systems like the Wadden Sea is believed to be primarily due to asymmetries in the tidal currents. Those asymmetries are driven either by barotropic effects, like tidal current asymmetries due to overtides ( $M_2$ – $M_4$  phase relation) and/or wind forcing, or by baroclinic effects related to the horizontal density gradient, where the latter are mainly caused by tidally asymmetric stratification or tidally asymmetric secondary circulation. Each of these mechanisms has potentially a strong impact on the vertical sediment distribution, on the one hand due to tidal asymmetries in the bottom-shear stress and on the other hand due to ebb-flood differences of internal mixing [*Burchard et al.*, 2013]. Therefore, the same processes that generate estuarine circulation may still substantially contribute to tidal pumping and thus to the net sediment flux.

Lateral circulation can also influence the along-channel sediment fluxes in a more direct way. At our site, we observe a persistent across-channel sediment flux, which is to a large fraction due to a residual secondary circulation. This flux is directed such that it transports sediment to regions of the channel, which are known to be generally more ebb dominated [*Becherer et al.*, 2015]. Therefore, the observed lateral flux is likely to contribute to an export of sediment in the channel. Arguments about the general implications of the lateral transport remain highly speculative since our point measurements do not provide enough information to properly reconstruct the sediment pathways and the complex interactions of lateral and longitudinal processes.

Besides the spatial limitations, we are also limited in time. The main drivers for sediment transport in the Wadden Sea are the tidal currents, wind, and the horizontal density gradient. All three forces change on a variety of time scales. The horizontal density gradient in the Wadden Sea varies substantially during the year, with changing relative importance of salinity and temperature [*Burchard et al.*, 2008; *Burchard and Badewien*, 2015]. During winter and fall, density differences are mainly due to salinity, whereas during dry springs (our observation window) or during hot summers they can be also dominated by temperature differences. Despite a strong seasonality, the density gradient is usually directed in such a way that it supports estuarine circulation [*Burchard and Badewien*, 2015]. The strength of the horizontal density gradients observed during our campaign lies well in the ballpark of annual average values, which implies that our observations of estuarine circulation are at least to some extent representative for typical Wadden Sea conditions.

Also the tidal currents change substantially on different time scales. Despite the fact that neap-spring differences in tidal amplitude are rather small at our site, *Bartholomä et al.* [2009] find that the amount of suspended sediment changes substantially during a neap-spring cycle. Furthermore, *Gräwe et al.* [2014] pointed out that both the  $M_2$ -tidal and  $M_4$ -tidal component have a significant seasonality. This is particularly important, since the phase relation of  $M_2$  and  $M_4$  controls a substantial fraction of the tidal pumping term [*Burchard et al.*, 2013], which we found to be the dominating term during calm conditions.

Therefore, our 5 day measurement window can only provide a snap-shot of the changing sediment dynamics of the Wadden Sea. This illustrates a general problem of observation-based sediment studies. We are only able to make quantitative statements for particular points in a system for a restricted period of time. Therefore, it seems difficult if not impossible to calculate reasonable sediment budgets for complicated systems like the Wadden Sea purely based on measurement data. This means that we are limited to rather qualitative and sometimes even speculative arguments about the entire system.

Despite those limitations, it is possible to draw some general conclusions. The along-channel exchange flow component is only a minor contributor to the sediment transport in the Wadden Sea. It is usually 1 order of magnitude smaller than tidal pumping or the barotropic flux due to wind. Nevertheless, many of the processes that are involved in the generation of estuarine circulation, like for instance barotropic tidal asymmetries ( $M_2$ – $M_4$  relation), internal mixing asymmetries (tidal straining), or lateral circulation, also significantly contribute to tidal pumping and thus to the dominating sediment transport term under calm conditions. Which of these different drivers however is the major control of tidal pumping in weakly stratified systems like the Wadden Sea, remains an open question for future studies.

### Acknowledgments

We are grateful to two anonymous reviewers, who helped to substantially improve the manuscript by their thoughtful comments. The present study has been carried out in the framework of the project ECOWS (Role of Estuarine Circulation for Transport of Suspended Particulate Matter in the Wadden Sea) funded by the German Research Foundation (DFG) as project BU1199/11 and by the German Federal Ministry of Research and Education in the framework of the project PACE (The future of the Wadden Sea sediment fluxes: still keeping pace with sea level rise?, FKZ 03F0634A). We gratefully acknowledge the technical assistance by Volker Mohrholz, Toralf Heene, Tim Juncker, Wilhelm Korrengk, Kaveh Purkiani (all IOW), Thomas Badewien (Oldenburg, Germany), and Alexander Bartholomä (Wilhelmshaven, Germany) as well as the crew of the R/V *Ludwig Prandtl*. The data are available from the authors upon request (jbecherer@coas.oregonstate.edu).

### References

- Baker, E. T., and J. W. Lavelle (1984), The effect of particle size on the light attenuation coefficient of natural suspensions, *J. Geophys. Res.*, *89*(C5), 8197–8203.
- Bartholomä, A., A. Kubicki, T. H. Badewien, and B. W. Flemming (2009), Suspended sediment transport in the German Wadden Sea—Seasonal variations and extreme events, *Ocean Dyn.*, *59*(2), 213–225.
- Becherer, J. (2014), Estuarine circulation in well-mixed tidal inlets, PhD thesis, Univ. Rostock, Rostock, Germany, doi:10.13140/RG.2.1.3144.4001.
- Becherer, J., H. Burchard, G. Flöser, V. Mohrholz, and L. Umlauf (2011), Evidence of tidal straining in well-mixed channel flow from micro-structure observations, *Geophys. Res. Lett.*, *38*, L17611, doi:10.1029/2011GL049005.
- Becherer, J., M. T. Stacey, L. Umlauf, and H. Burchard (2015), Lateral circulation generates flood tide stratification and estuarine exchange flow in a curved tidal inlet, *J. Phys. Oceanogr.*, *45*(3), 638–656.
- Burchard, H., and T. H. Badewien (2015), Thermohaline residual circulation of the Wadden Sea, *Ocean Dyn.*, *65*(12), 1717–1730.
- Burchard, H., and R. D. Hetland (2010), Quantifying the contributions of tidal straining and gravitational circulation to residual circulation in periodically stratified tidal estuaries, *J. Phys. Oceanogr.*, *40*, 1243–1262.
- Burchard, H., G. Flöser, J. V. Staneva, T. H. Badewien, and R. Riethmüller (2008), Impact of density gradients on net sediment transport into the Wadden Sea, *J. Phys. Oceanogr.*, *38*(3), 566–587.
- Burchard, H., R. Hetland, E. Schulz, and H. Schuttelaars (2011), Drivers of residual estuarine circulation in tidally energetic estuaries: Straight and irrotational channels with parabolic cross section, *J. Phys. Oceanogr.*, *41*(3), 548–570.
- Burchard, H., H. M. Schuttelaars, and W. R. Geyer (2013), Residual sediment fluxes in weakly-to-periodically stratified estuaries and tidal inlets, *J. Phys. Oceanogr.*, *43*(9), 1841–1861.
- Dronkers, J. (1986), Tidal asymmetry and estuarine morphology, *Neth. J. Sea Res.*, *20*(2), 117–131.
- Flöser, G., H. Burchard, and R. Riethmüller (2011), Observational evidence for estuarine circulation in the German Wadden Sea, *Cont. Shelf Res.*, *31*, 1633–1639.
- Flöser, G., R. Riethmüller, J. Nauw, and H. Burchard (2013), Observational evidence for the general presence of estuarine circulation in the Wadden Sea, *J. Coastal Res.*, *65*, 1527–1532.
- Geyer, W. R., J. D. Woodruff, and P. Traykovski (2001), Sediment transport and trapping in the Hudson River estuary, *Estuaries*, *24*(5), 670–679.
- Gräwe, U., H. Burchard, M. Müller, and H. Schuttelaars (2014), Seasonal variability in  $M_2$  and  $M_4$  tidal constituents and its implications for the coastal residual sediment transport, *Geophys. Res. Lett.*, *41*, 5563–5570, doi:10.1002/2014GL060517.
- Hansen, D. V., and M. Rattray (1965), Gravitational circulation in straits and estuaries, *J. Mar. Res.*, *23*, 104–122.
- Jay, D., and J. Musiak (1994), Particle trapping in estuarine tidal flows, *J. Geophys. Res.*, *99*(C10), 20,445–20,461.
- Lerczak, J., and W. Geyer (2004), Modeling the lateral circulation in straight, stratified estuaries, *J. Phys. Oceanogr.*, *34*(6), 1410–1428.
- McSweeney, J. M., R. J. Chant, and C. K. Sommerfield (2016), Lateral variability of sediment transport in the Delaware estuary, *J. Geophys. Res.*, *121*, 725–744, doi:10.1002/2015JC010974.
- Purkiani, K., J. Becherer, G. Flöser, U. Gräwe, V. Mohrholz, H. M. Schuttelaars, and H. Burchard (2015), Numerical analysis of stratification and destratification processes in a tidally energetic inlet with an ebb tidal delta, *J. Geophys. Res.*, *120*, 225–243, doi:10.1002/2014JC010325.
- Purkiani, K., J. Becherer, K. Klingbeil, and H. Burchard (2016), Wind-induced variability of estuarine circulation in a tidally energetic inlet with curvature, *J. Geophys. Res. Oceans*, *121*, doi:10.1002/2015JC010945, in press.
- Schulz, E., H. M. Schuttelaars, U. Gräwe, and H. Burchard (2015), Impact of the depth-to-width ratio of periodically stratified tidal channels on the estuarine circulation, *J. Phys. Oceanogr.*, *45*, 2048–2069.
- Schulz, K., and L. Umlauf (2016), Residual transport of suspended material by tidal straining near sloping topography, *J. Phys. Oceanogr.*, doi:10.1175/JPO-D-15-0218.1, in press.
- Scully, M. E., and C. T. Friedrichs (2007), Sediment pumping by tidal asymmetry in a partially mixed estuary, *J. Geophys. Res.*, *112*, C07028, doi:10.1029/2006JC003784.
- Sommerfield, C. K., and K. C. Wong (2011), Mechanisms of sediment flux and turbidity maintenance in the Delaware Estuary, *J. Geophys. Res.*, *116*, C01005, doi:10.1029/2010JC006462.
- Stacey, M. T. (1996), Turbulent mixing and residual circulation in a partially stratified estuary, PhD thesis, Stanford Univ., Stanford, Calif.
- Stanev, E., G. Flöser, and J. Wolff (2003), First- and higher-order dynamical controls on water exchanges between tidal basins and the open ocean. A case study for the East Frisian Wadden Sea, *Ocean Dyn.*, *53*(3), 146–165.
- van der Lee, E., and L. Umlauf (2011), Internal wave mixing in the Baltic Sea: Near-inertial waves in the absence of tides, *J. Geophys. Res.*, *116*, C10016, doi:10.1029/2011JC007072.